MATERIALS SCIENCE

Stretchable batteries with gradient multilayer conductors

Minsu Gu[1,2]*, Woo-Jin Song[3]*, Jaehyung Hong[4], Sung Youb Kim[4], Tae Joo Shin[5], Nicholas A. Kotov[2,6]†, Soojin Park[3]†, Byeong-Su Kim[1]†

Stretchable conductors are essential components in next-generation deformable and wearable electronic devices. The ability of stretchable conductors to achieve sufficient electrical conductivity, however, remains limited under high strain, which is particularly detrimental for charge storage devices. In this study, we present stretchable conductors made from multiple layers of gradient assembled polyurethane (GAP) comprising gold nanoparticles capable of self-assembly under strain. Stratified layering affords control over the composite internal architecture at multiple scales, leading to metallic conductivity in both the lateral and transversal directions under strains of as high as 300%. The unique combination of the electrical and mechanical properties of GAP electrodes enables the development of a stretchable lithium-ion battery with a charge-discharge rate capability of 100 mAh g^{-1} at a current density of 0.5 A g^{-1} and remarkable cycle retention of 96% after 1000 cycles. The hierarchical GAP nanocomposites afford rapid fabrication of advanced charge storage devices.

INTRODUCTION

The rapid development of stretchable biomimetic electronics has been fueled by a growing demand for wearable health care devices, electronic skin, artificial muscles, and neuroprosthetic implants (*1*–*5*). The foundational condition for broadening the spectrum of these devices is the availability of stretchable conductors that have high electrical conductivity under large mechanical strain (*6*–*8*). Diversification of the biomimetic electronics presents researchers with a challenge in designing materials with an increasing number of demanding combinations of stretchability, conductivity, and surface electrochemistry that are not present in classical and nanostructured materials represented by composites from nanoscale forms of carbon and metals (*9*–*15*). Furthermore, similar demands for materials with nearly impossible combinations of properties have emerged in other areas of technology, and new approaches realizing these materials are needed.

Two strategies are used most often to design stretchable conductors. In the first methodology, conductive nanoscale components are deposited onto the surface of an elastomeric substrate to mitigate the loss of conductivity upon deformation (*16*). The surfaces of these stretchable conductors display buckled (*17*, *18*), wrinkled (*19*), waved (*20*), crumpled (*21*) island structures (*22*) or patterned interconnects (*23*, *24*) that accommodate mechanical stress while maintaining the percolation threshold. These three-dimensional (3D) geometries are favorable for combining ultimate strain and stable electrical properties under physical deformations, but low volume of the conducting layer, complexity of the manufacturing process, and ease of damage hamper the applicability of these structures.

In the second strategy, polymer nanocomposites acquire conductive pathways owing to conductive fillers dispersed in the bulk of the elastomeric polymers (*7*, *11*–*14*). The advantages of these composites include the ability to carry a high current and self-heal. High-throughput fabrication of composites containing a variety of nanoparticles (NPs), nanowires, and nanotubes is also possible. However, the contrarian relationship between stretchability and conductivity is more pronounced for these composites than for 3D coatings. For example, composites with a high elastomer content typically display an acceptable strain behavior but low intrinsic conductivity. On the other hand, the high loading of a stiff conductive component leads to low strain because a mechanical failure of these materials occurs on stress-concentrated hard segments, which promotes the propagation of nano- and microcracks in the nanocomposites (*25*). The self-organization of nanoscale components in a polymeric matrix, which results in an entropy-driven formation of the conductive bands of NPs at high strain, can mitigate this problem (*14*). A comparatively low volumetric content of the filler as compared to traditional nanocomposites results in a substantial reduction of the stiffening effect and high stretchability. Among the latest developments in this research area are kirigami conductors that completely eliminate the dependence of the conductance on strain (*26*). A zero conductance gradient upon strain is achieved by making periodic cuts in the stiff conductor, thereby eliminating the local concentration of strains, causing a material failure. However, kirigami conductors share certain disadvantages of 3D conductive coatings, including a complex manufacturing process and fragility.

Therefore, the problem of how to engineer the composites combining high conductivity and stretchability remains acute. Some of the best stretchable conductors are made by vacuum-assisted filtration (VAF) and layer-by-layer (LbL) assembly (*27*–*33*). These conductors can be applied to a variety of nanoscale components including graphene and gold NPs (*34*, *35*). LbL assembly can manufacture highly ordered architectures, allowing fine nanoscale control over the thickness and composition of hybrid multicomponents through a sequential assembly enabling higher conductance (*30*, *32*). VAF composites also afford some level of nanoscale control and generally provide greater strain (*14*). Since both charge transport and mechanical deformations must involve multiple scales of structural optimization, these and other material engineering techniques can benefit from structural control and multiple scales integrating nano-, micro-, and macroscale organization.

[1]Department of Chemistry, Yonsei University, Seoul 03722, Republic of Korea. [2]Department of Chemical Engineering, University of Michigan, Ann Arbor, MI 48109, USA. [3]Department of Chemistry, Division of Advanced Materials Science, Pohang University of Science and Technology (POSTECH), Pohang 37673, Republic of Korea. [4]Department of Mechanical Engineering, Ulsan National Institute of Science and Technology (UNIST), Ulsan 44919, Republic of Korea. [5]UNIST Central Research Facilities (UCRF), UNIST, Ulsan 44919, Republic of Korea. [6]Michigan Institute of Translational Nanotechnology, 3233 Andora Drive, Ypsilanti, MI 48198, USA.
*These authors contributed equally to this work.
†Corresponding author. Email: kotov@umich.edu (N.A.K.); soojin.park@postech.ac.kr (S.P.); bskim19@yonsei.ac.kr (B.-S.K.)

Here, we report a nanocomposite that combines the advantages of both types of stretchable conductors discussed above while mitigating many of their disadvantages. Our material engineering strategy involves the realization of a hierarchical internal architecture controlled at multiple scales. Individual composite sheets of this material are designed as a gradient assembled polyurethane (GAP)–based stretchable conductor using negatively charged Au NPs and positively charged water-dispersible polyurethane (PU) that control both nano- and mesoscale organization of the material (Fig. 1). The micro- and macroscale organization of the composite is accomplished through the layering of separate composite sheets containing Au NPs at various ratios. These GAP stretchable multilayer conductors demonstrate (i) a top-surface conductive structure with a mechanical stretchability of greater than 300% strain for a high-gradient architecture and (ii) a through-plane conductivity from the top to the bottom surface of the conductor by increasing the number of interlayers for a low-gradient architecture. As a demonstration of their fundamental advantages and technological significance, GAP composites make possible the construction of a stretchable energy storage device in the form of a lithium-ion battery that retains its stable electrochemical performance under exceptionally high rates of strain. Hierarchical multiscale engineering of the conductive composites offers conceptual insight into the design of various materials for future energy conversion and storage devices, as well as biomimetic electronics.

RESULTS

Fabrication of GAP conductors

Negatively charged Au NPs stabilized by citrate served as the conductive component of the stretchable conductors in this work. The average

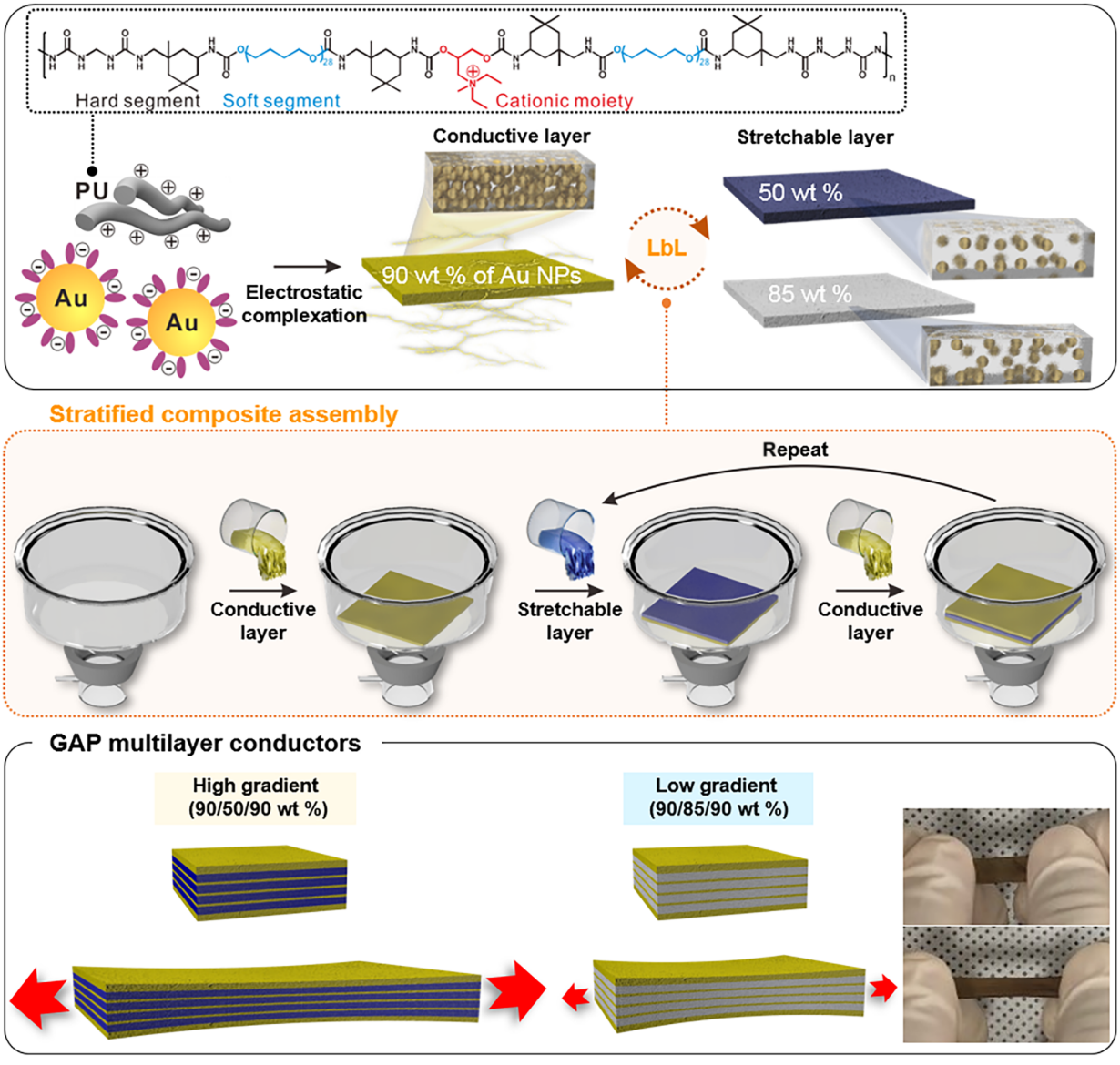

Fig. 1. Schematic illustration of GAP multilayer conductors. Stratified assembly of stretchable nanocomposites with different concentrations of Au NPs in the elastic layer. The interface boundary of the layered structure is stratified by the sequential filtration of each AuPU composite suspension with different concentration gradients. The photographs show a GAP multilayer conductor under relaxed and strained conditions. (Photo credit: Woo-Jin Song, Pohang University of Science and Technology)

diameter of the Au NPs was 21.5 ± 5.3 nm (fig. S1). Although nanowires and nanotubes are known to be suitable candidates for stretchable conductors owing to their high aspect ratio, NPs can exhibit a greater degree of freedom within a polymer matrix under strain, in addition to their facile and scalable synthesis (*14*). A positively charged water-dispersible PU suspension was used as an elastomeric component for fabricating the stretchable conductors.

Initially, we prepared a nanocomposite suspension through the mixing of Au NPs and PU suspensions at controlled ratios of 50 to 90 weight % (wt %) of the Au NPs (fig. S2). This colloidal composite is denoted hereafter as AuPU followed by the wt % of the Au NPs. A neat PU film displayed a stretchability of as high as 615%. Increasing the content of Au NPs within the PU matrix from 50 wt % to 85 and 90 wt % led to a sharp decrease in the stretchability of the AuPU composite films to 380, 140, and 2%, respectively. In contrast, the resistance decreased significantly; for example, the 90 wt % AuPU composite film demonstrated a resistance of less than 1 ohm corresponding to an electrical conductivity of 1.57×10^4, which is comparable to that of a metal conductor (fig. S3). This film also exhibited excellent durability, namely, no change in resistance was observed for 100 bending cycles (fig. S2). Nevertheless, we were unable to achieve both a high stretchability of greater than 100% and metallic conductivity in a single-layered nanocomposite films at the same time.

Therefore, to combat the limitations related to the conductivity and stretchability of each single-layered AuPU nanocomposite film, we used a novel geometric AuPU film design with stratified multilayers of single AuPU nanocomposite films assembled using both conventional VAF and LbL assembly. Specifically, a 90 wt % AuPU film was selected as the conductive layer at both the top and bottom outermost surfaces, with either a 50 or 85 wt % AuPU film as a stretchable layer in between. This novel design affords a high-gradient (i.e., 90 and 50 wt % AuPU) and a low-gradient (i.e., 90 and 85 wt % AuPU) multilayer structure of distributed Au NPs throughout both conductors. This multilayered structure is referred to as a three-layer stratified GAP conductor (3 L). Furthermore, to investigate the effect of multilayers with a fixed Au NP content, multilayer conductor interlayers were evenly divided further into different numbers of layers by adding more conductive layers between the stretchable layers while fixing the contents of the multilayer conductors from 5 L to 9 L with a total of three conductive layers and one stretchable layer. The specific contents of the Au NPs in the high- and low-gradient multilayer conductors were nearly identical at 75 and 88 wt %, respectively, as confirmed by thermogravimetric analysis (TGA) (fig. S4). These results suggest that it is possible to precisely control the number of layers and gradient distribution of the hierarchical multiscale composite without altering the compositional ratio of each conductive filler and elastic polymer.

The successful fabrication of these GAP multilayer conductors was confirmed through cross-sectional scanning electron microscopy (SEM) (Fig. 2). Multilayered architectures were observed through the relative contrast between the Au NPs and PU in each nanocomposite layer. Corresponding energy-dispersive x-ray spectroscopy images also revealed the gradient distribution of Au and carbon, indicating that both Au NPs and PU were distributed throughout the entire conductor and exhibited a concentration gradient.

Characterization of GAP multilayer conductors

Stratified conductors with a high gradient exhibited a stretchability of greater than 300%, whereas the stretchability of low-gradient stratified conductors exhibited less than 100% strain (Fig. 3A). The rupture point of both high and low GAP conductors gradually decreased. As the number of interlayers increased, the Young's modulus increased (Fig. 3, B and C). The Young's moduli of the high-gradient stratified conductors were lower than those of the low-gradient stratified conductors, indicating that the high ratio of Au NPs to PU in low-gradient conductors induced stiff and rigid nanocomposites, resulting in inferior stretchability.

We investigated the change in GAP conductor morphology and internal structure under strain by SEM. The top-surface images showed 3D interconnected microporous networks of Au NP-anchored PU chains (fig. S5). Although the porosity increased because of enlarged voids and cracks under strain, good structural recovery of the AuPU nanocomposites, originating from the robust PU, was observed. However, some stress failure of stratified GAP conductors due to nano- and microcracks in the nanocomposites was confirmed by the cross-sectional SEM images of the 9 L high-gradient multilayer conductor under strain (fig. S6). A partially broken interlayer was observed at exactly the same middle layer of each conductor. These results explain the electrically conductive surface as well as the outstanding structural recovery by preventing a rupture of the conductive layer at the outermost sides of both the top and bottom surfaces without severe cracking. In addition, because of the high affinity and the compatibility of the identical and homogeneous components in each nanocomposite layer as shown in fig. S7, there was no delamination of layers from the bottom layer. It should be highlighted that the stratified composites can be used to fabricate a mechanically powerful stretchable conductor using a simple and scalable solution process.

To further verify the rupture point of the GAP multilayer conductors through crack propagation starting from the interlayers, we conducted a mechanical simulation of the stress distribution in the horizontal and vertical directions in 5 L and 9 L low GAP multilayer conductors using the ABAQUS software package. The horizontal stress, σ_x, of the 9 L conductor, along with the stretching direction, was higher than that of the 5 L conductor (Fig. 3D), whereas the vertical stress, σ_z, of the 9 L conductor decreased significantly to −40.5 kPa (i.e., compression) (Fig. 3E). This indicates that the rupture point of the GAP conductors decreased with an increasing number of interlayers, which corresponds with the results shown in Fig. 3 (A to C). In addition, a higher stress was concentrated in the middle and center layers than in the outer layers. As a result, concentrated stress in the middle layer initiated the rupture of the GAP conductor, rather than starting from the outside conductive layer, which is consistent with previous cross-sectional SEM images (fig. S7). We then examined the stress distribution with a crack in the middle and center layers of the 9 L low GAP conductor (fig. S8). As a result, strong σ_x is focused on the end of the crack, which leads to shorter rupture point and possible further crack propagation. In the multilayer structure, however, the crack is rather deflected to increase the length of propagation path than vertically propagates, eventually causing the crack to be arrested (*36*). Accordingly, this observation indicates that the multilayered architecture is advantageous for mitigating crack propagation from the stress concentration under stretching.

The electrical conductivity of all GAP multilayer conductors showed a similar change in resistance regardless of the number of interlayers and gradient assembly because they all had an identical top conductive layer composed of 90 wt % AuPU nanocomposite (Fig. 4A and fig. S3B). We also performed a durability test of the electrical conductivity for the GAP multilayer conductors under strains of 20, 30,

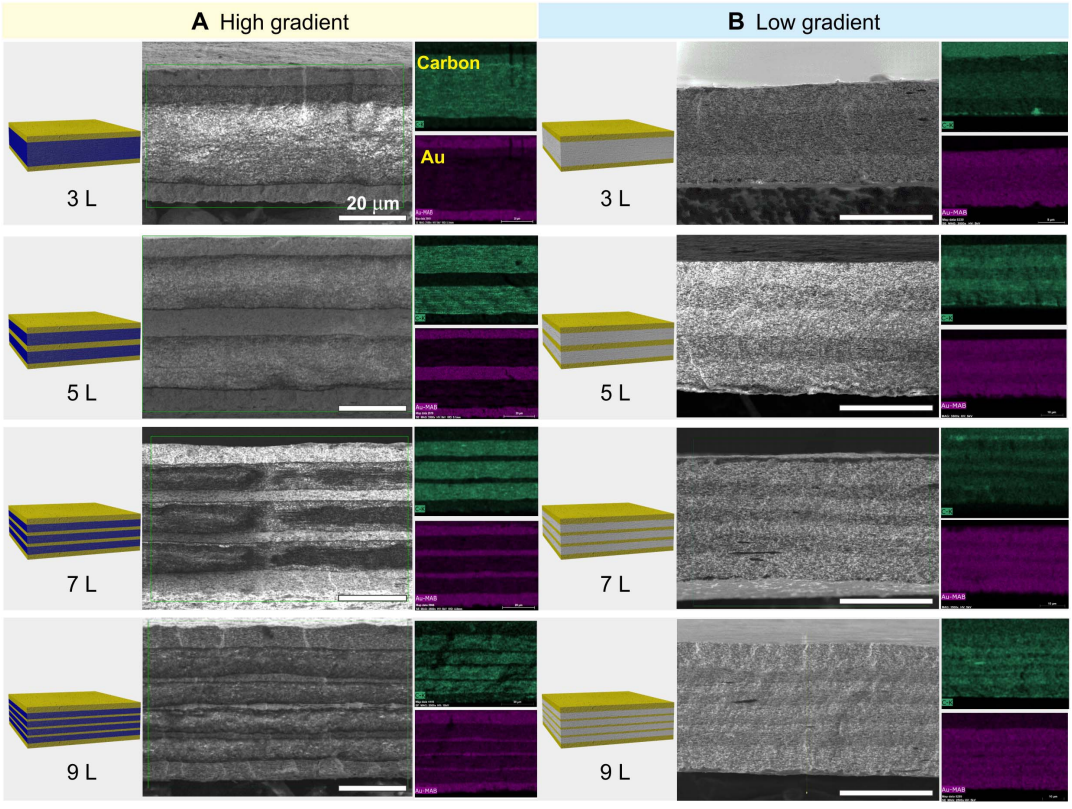

Fig. 2. Architecture-controlled GAP multilayer conductors. Schematic illustrations and representative cross-sectional SEM images with elemental mapping images of carbon and Au of (**A**) high-gradient (90/50/90 wt % AuPU) and (**B**) low-gradient (90/85/90 wt % AuPU) multilayer conductors with an increasing number of layers. Scale bars, 20 μm.

and 40% (fig. S9), which showed highly stable performance retention even after 1000 cycles. These outstanding mechanical and electrical properties demonstrate the unique ability of a high-gradient architecture with an in-plane structure to achieve both metallic top-surface conductivity and stretchability.

It is also important to consider the electrical connection of the interlayers under strain. The high GAP stratified conductor has a limitation, however, in that only the top surface is conductive as a conventional geometrically designed conductor. In contrast, the low GAP multilayer conductor is fully conductive from the top to the bottom surface with a low vertical (transversal) direction resistance of ~50 ohms measured in the 3 L low-gradient stratified conductors, although its tensile strength was much lower than those of GAP composites with a high gradient.

The vertical conductivity in low-gradient stratified conductors was theoretically calculated to prove the existence of a conductive pathway through the stretchable layer as a function of the number of interlayers (Fig. 4B). The vertical conductivity was increased by increasing the number of interlayers, facilitating through-plane electrical conduction from the top to bottom surfaces. In addition, the change in vertical conductivity in the 5 L and 9 L of low-gradient stratified conductors was also investigated by considering the strain-dependent conductivity of each layer (Fig. 4C). In contrast to the horizontal conductivity results on the top surface of the conductor, the conductivity in the vertical direction increased with an increasing number of interlayers, verifying that increasing the number of interlayers is advantageous for electrical conductivity.

Electrical conductivity is strongly related to the connectivity between conductive fillers; to retain stable electrical conductivity in a stretchable conductor, the behavior of the conductive filler under strain is important. In this regard, in situ small-angle x-ray scattering (SAXS) is a method for better understanding the behavior of conductive fillers in an elastomer matrix (Fig. 4, D to F, and S10) (*7*). SAXS analyses of samples were conducted at a constant stretching rate of 80 μm s^{-1} under a range of strain of 0 to 100%. Figure 4E shows the 2D SAXS patterns of pure PU and 50 wt % AuPU nanocomposite films at applied uniaxial strains of 0, 50, and 100%. In the initial unstrained state, 2D patterns of pure PU and AuPU nanocomposite films exhibited an isotropic scattering geometry, indicating a random dispersion of the hard segments of the PU and Au NPs. However, the two samples began to develop different scattering patterns upon stretching. The patterns of the pure PU film evolved from circular to elliptical shapes while under strain, indicating that the hard segments of PU were aligned along the stretching direction (Fig. 4E) (*37*). In contrast, the AuPU nanocomposite film showed a butterfly-like pattern upon stretching, resulting from the nonaffine relative displacements of Au NPs in the polymer matrix under strain (*38*). Note that Au NPs in the nanocomposite have a higher electron density than the PU matrix, demonstrating that the SAXS patterns of the nanocomposite are derived from the Au NPs. As the strain increased, the Au NPs gradually formed clusters of raft-like structures perpendicular to the strain axis owing to the Poisson contraction, leading to banded Au NP clusters aligned in the stretching direction. These phenomena may lead to significant alignment and increased interconnection of Au

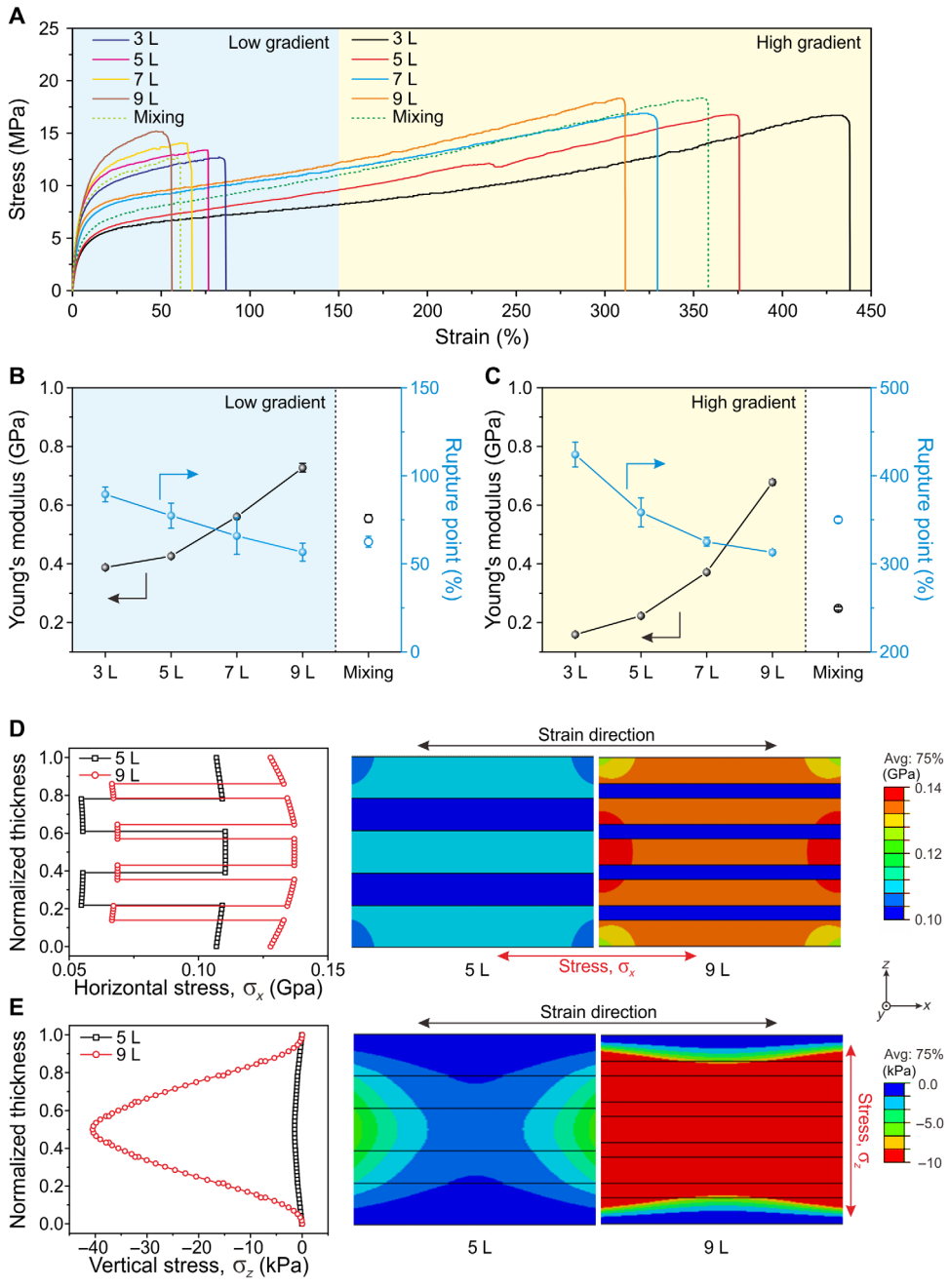

Fig. 3. Mechanical properties of GAP multilayer conductors. (**A**) Stress-strain curves for all GAP multilayer conductors. (**B** and **C**) Young's modulus and rupture point of low and high GAP multilayer conductors. Finite element analysis of (directional) stress distribution in the (**D**) horizontal and (**E**) vertical directions for 5 L and 9 L low GAP conductors under 50% strain.

NPs under uniaxial strain, resulting in the effective maintenance of its electrical conductivity under strain (*39*).

Moreover, to quantitatively investigate the degree of self-assembly of AuPU into conducting bands in nanocomposite films along the stretching direction, we calculated Herman's orientation factor, (f)

$$f = \frac{3(\cos^2\varphi) - 1}{2}, (\cos^2\varphi) = \frac{\int_0^{\pi/2} I(\varphi)\cos^2\varphi \sin\varphi \, d\varphi}{\int_0^{\pi/2} I(\varphi)\sin\varphi \, d\varphi}$$

where f is the orientation factor, varying from 0 to 1 for isotropic and perfectly perpendicular to the strain direction, respectively, and φ is the azimuthal angle. When strain is applied, the alignment quality of PU increases along the stretching direction owing to the orientation of the segment domains (Fig. 4F). In contrast, the orientation factor of AuPU shows that the percolation network in the stretching direction began to collapse at a strain of 80%, which is consistent with the rapidly increasing point of resistance shown in Fig. 4A.

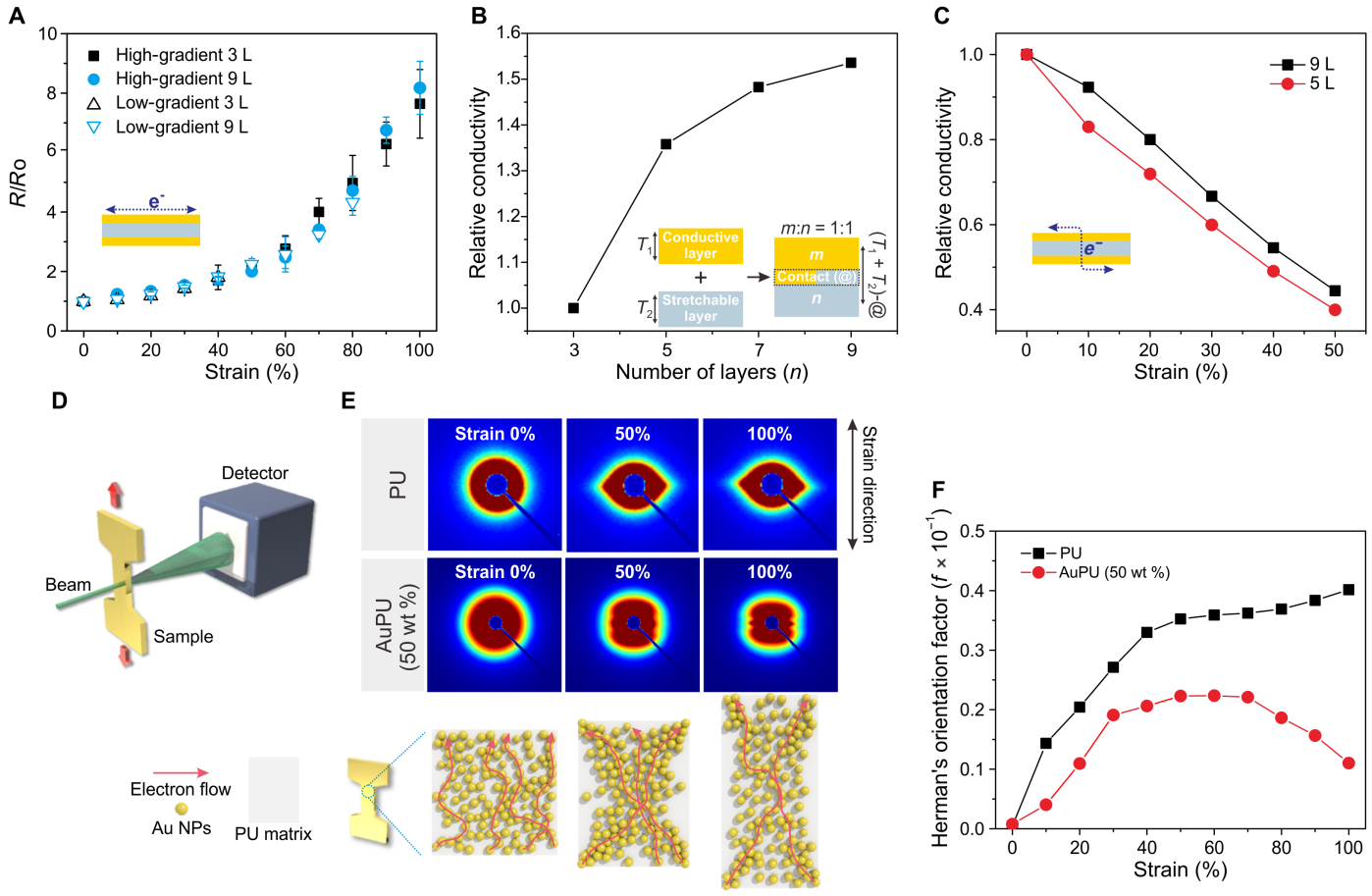

Fig. 4. Electrical properties of GAP multilayer conductors and small-angle x-ray scattering analysis for the percolation network of Au NPs in a PU matrix under strain. (**A**) Normalized resistance on the top surface of high and low GAP multilayer conductors of 3 L and 9 L under different strain conditions. (**B**) Calculation of vertical conductivity for low GAP conductors with increasing number of layers. (**C**) Change in vertical conductivity in 5 L and 9 L low GAP conductors under strain. (**D**) Schematic illustration of the experimental setup of in situ small-angle x-ray scattering (SAXS) measurement. (**E**) 2D SAXS patterns at selected uniaxial strains of 0, 50, and 100% for pure PU and 50 wt % AuPU nanocomposite films, and schematic illustrations summarizing the behavior of Au NPs (yellow spheres) in the matrix and changes in the electrical pathway (red lines) under strain determined by SAXS analysis. (**F**) Calculated Herman's orientation factor, *f*, under strain for a single layer of PU and 50 wt % AuPU.

Electrochemical performance

To confirm the practical application of the stretchable GAP multilayer conductor as a current collector electrode, the electrochemical performance of an aqueous rechargeable lithium-ion battery as a potential power source was examined. The aqueous rechargeable lithium-ion battery has a high-rate capability as a result of the fast transport of Li ions due to the use of aqueous electrolytes instead of conventional organic electrolytes, which renders the batteries extremely safe from the risk of explosion (*40*, *41*). Initially, we synthesized the active materials on the surface of carbon nanotubes for the anode and the cathode, namely, polyimide/carbon nanotubes (PI/CNTs) (*42*) and lithium manganese oxide ($LiMn_2O_4$)/carbon nanotubes (LMO/CNTs) (*43*), respectively (see figs. S11 and S12). To fabricate a stretchable electrode, the prepared cathode and anode materials were deposited onto the high GAP multilayer conductors (denoted as GAP cathode and GAP anode, respectively; fig. S13) through a spray coating process. Although these active materials showed some microcracks under 30% strain, the active materials recovered to their original state after releasing the strain, demonstrating their superior mechanical and electrochemical stability (fig. S14).

The electrochemical performance of the GAP electrode was determined through cyclic voltammetry (CV) using a three-electrode system with a 1 M Li_2SO_4 electrolyte. In Fig. 5A, CV curves of the GAP anode and GAP cathode with an increasing scan rate showed typical redox peaks of PI and LMO (*7*). Thus, the GAP multilayer conductor indicated the electrochemical stability within the working voltage range, demonstrating that the GAP multilayer conductor can be used as a current collector for this battery system. Figure 5B displays voltage profiles of the GAP cathode between 0.0 and 1.2 V at various current densities. Specific capacities of 132 and 102 mAh g^{-1} were delivered at 1 and 5 A g^{-1}, respectively. The rate performance of the GAP anode at various current rates ranging from 2 to 15 A g^{-1} within a voltage window of 0.0 to −1.0 V is presented (Fig. 5C). The GAP anode can deliver 95 mAh g^{-1}, even at a high current density of 15 A g^{-1}. Moreover, both the GAP cathode and GAP anode showed outstanding cycling performances at current densities of 5 and 10 A g^{-1}, respectively, after 200 cycles (fig. S15). We also confirmed that the active materials were still firmly attached to the surface of the GAP conductor without any significant damage after cycling performance (fig. S16).

The electrochemical performance of a full cell consisting of a GAP cathode and GAP anode with an aqueous electrolyte was evaluated for a voltage range of 0.0 to 2.2 V without any applied strain. The discharge capacities of the full cell were 100 mAh g^{-1} at a current density of 0.5 A g^{-1}; their discharge times are about 2 min (figs. S17 and S18). Furthermore, the long-term cycle performance of the full cell showed highly stable cycle retention of 96% at a current density of 0.5 A g^{-1} even after 1000 cycles (Fig. 5D).

More specifically, to demonstrate the electrochemical performance under strain, we designed the stretchable aqueous rechargeable lithium-ion battery to be practically feasible for deformable electronic devices (Fig. 5E). Recovery properties of the proposed battery could be introduced using the packaging materials of polydimethylsiloxane (PDMS) (fig. S19). This stretchable aqueous rechargeable lithium-ion battery was cycled at a current density of 0.5 A g^{-1} between 0 and 30% strain (Fig. 5F); at 30% strain, the stretchable aqueous rechargeable lithium-ion battery showed an outstanding capacity retention of 72% for 10 cycles, as compared to the unstrained conditions. After releasing the strain, the specific capacity of the stretchable aqueous rechargeable lithium-ion battery completely recovered its initial values. To further investigate the electrochemical stability of the stretchable battery, we determined the cycling performance at a current density of 0.5 A g^{-1} while being subjected to 20 stretching cycles at a strain of 30% per 20 cycles (Fig. 5G). Figure 5H shows that a stretchable battery connected in series can light up orange light-emitting diodes (LEDs) while stretching under 30% strain (fig. S20 and movie S1). These results demonstrate that stretchable full battery–based GAP stretchable conductors are an appropriate power source for various stretchable electronic devices.

DISCUSSION

GAP composites offer a new degree of freedom in resolving the optimization of a complex set of property correlations of classical and hybrid materials. Their stratified design methodology enables control over the mechanical and charge transport properties by changing the material architecture from the nanoscale to the macroscale. As a representation of new capabilities emerging in these composites, controlling the spatial distribution of the charge transport pathways becomes possible as exemplified by the variation in the primary charge transport pathways in low- and high-gradient GAP conductors. Furthermore, we also demonstrated that these materials

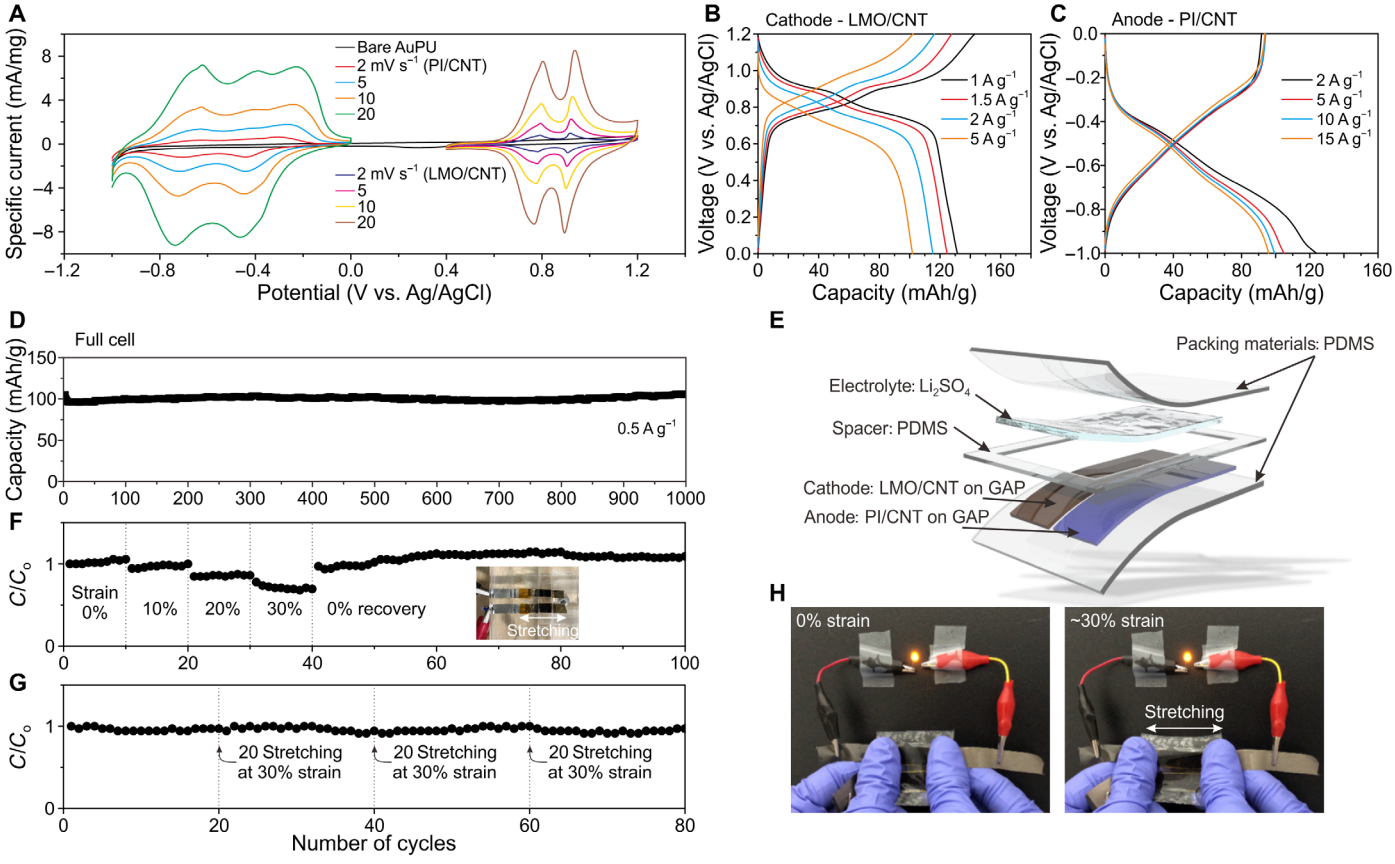

Fig. 5. Electrochemical performance of stretchable aqueous rechargeable lithium-ion battery using a GAP multilayer conductor as a current collector. (**A**) CV profiles of the GAP anode (PI/CNT) and GAP cathode (LMO/CNT) at various current densities in three electrode systems in a 1 M Li_2SO_4 electrolyte with a Pt electrode and an Ag/AgCl electrode as the counter and reference electrodes, respectively. (**B** and **C**) Galvanostatic charge-discharge curves of the GAP cathode and GAP anode, respectively. (**D**) Cycling performance of the full battery at a current density of 0.5 A g^{-1} between 0.0 and 2.2 V in 1 M Li_2SO_4 for 1000 cycles. (**E**) Schematic illustration of the stretchable aqueous rechargeable lithium-ion battery fabricated using the GAP anode and cathode with a coplanar layout. (**F**) Cycle performance of the stretchable full cell at a current density of 0.5 A g^{-1} under various strains of 0 to 30% for 100 cycles. (**G**) Capacity retention as a function of cycle at a current density of 0.5 A g^{-1}. The stretchable battery was pulled 20 times at a strain of 30% for each group of 20 electrochemical cycles. (**H**) Photographs of an LED bulb operated using stretchable aqueous lithium-ion battery under strains of 0 and 30%. (Photo credit: Woo-Jin Song, Pohang University of Science and Technology)

make possible a stretchable aqueous rechargeable lithium-ion battery, which delivers stable power with a high-rate capability under high strain. The multiscale hierarchical approach is versatile and can be further extended, not only in the fabrication of flexible and wearable electronics but also for other devices requiring challenging combinations of charge transport and mechanical properties represented by damage-resistant batteries.

MATERIALS AND METHODS

Materials

A 30 volume % cationic PU aqueous dispersion with a molecular mass of approximately 92,000 (Hepce Chem, Korea) and a multi-walled CNT with a diameter of 10 to 15 nm and a length of ~200 μm (Hanwha Nanotech Corp., Korea) were used in this study. Gold (III) chloride trihydrate ($HAuCl_4 \cdot 3H_2O$) was purchased from Sigma-Aldrich.

Synthesis of Au NPs

Gold (III) chloride trihydrate (360.0 mg) was added to 500 ml of deionized (DI) water. The gold precursor solution was heated to 95°C under vigorous stirring for 20 min. Subsequently, 100 ml of sodium citrate solution (34 mM) was added to the mixture. The aqueous solution was heated for 20 min and then cooled to room temperature.

Fabrication of single-layered AuPU nanocomposites

A 1.0 volume % aqueous PU solution of 0.50, 1.0, or 4.0 ml was slowly added to 250 ml of a prepared Au NP dispersion to achieve Au NP contents of 90, 85, or 50 wt % in AuPU, respectively, while stirring, followed by additional stirring for 5 min. Each mixture was filtered under vacuum using filter paper with a pore size of 0.8 μm and a diameter of 47 mm. The resultant film was peeled off the filter paper after completely drying the film for 1 day at room temperature.

Fabrication of stratified assembled GAP multilayer conductors

The stratified assembled multilayer architecture was constructed through the alternating physical filtration of single-layered AuPU nanocomposites under vacuum. Initially, a 90 wt % AuPU nanocomposite mixture used as a conductive layer was filtered, followed by 50 or 85 wt % AuPU nanocomposite mixtures used as stretchable layers. Last, the 90 wt % AuPU nanocomposite conductive layer was filtered again to produce 3 L high-gradient (i.e., 90/50/90 wt %) and low-gradient (i.e., 90/85/90 wt %) multilayer conductors. To fabricate a more layered structure with interlayers of greater than 3 L, the stretchable layer mixture was alternately and evenly filtered with one additional mixture of 90 wt % in AuPU while fixing the conductive layer contents at 90 wt % at the outermost sides of both the top and bottom surfaces.

Numerical simulation of GAP multilayer conductors

For finite element simulations conducted to demonstrate the mechanical and electrical properties of the multilayer conductors, we used Abaqus/Standard 6.14 software (Dassault Systémes). Static linear elastic analysis was conducted to describe the stress distribution of a layer under uniaxial tension. 2D plane strain quadratic elements were adopted, and we used material properties of stretchable and conductive layers based on experimental measurement in this study. We confirmed the convergence of the final solution with a different number of elements and a different number of loading steps. To exclude any delamination effect at the interface of the model, each interface between stretchable and conductive layers is perfectly tied without cohesive response. In addition, an electrical conduction analysis was implemented to identify the change in vertical conductivity of the multilayer conductors. Steady-state analysis was performed in both analyses. The contact layer between the conductive and stretchable layers was considered under the assumption of a contact 1:1 ratio. The elastic properties of each layer in the conductor, the dimensions of the multilayer conductors, and the strain-dependent electrical properties, which were measured experimentally, were adopted in all simulations. The thickness of the stretchable layer (i.e., resistance) was slightly decreased with an increase in the number of interlayers, as shown in the SEM images (Fig. 2). For the low GAP conductor, the thickness of the whole conductor and each stretchable layer for 5 L and 9 L interlayers are 27.42 and 4.71 μm and 27.17 and 2.06 μm, respectively.

Synthesis of active materials

In a typical experiment, 100 mg of CNT and 250 mg of $KMnO_4$ (Sigma-Aldrich) were mixed together in an agate mortar. The mixed powder was then poured into 100 ml of water and stirred for 10 min. A total of 0.5 ml of H_2SO_4 (95%, Samchun) was added to the above mixture with an extra 30 min of stirring. The mixture was then heated in an oil bath at 80°C while stirring for 1 hour. The precipitate was collected through filtration and washed repeatedly with DI water and ethanol. The product was then dried in an oven at 60°C for 12 hours to obtain MnO_2/CNT. To make the LMO/CNT, 0.25 g of the prepared MnO_2/CNT and 0.26 g of $LiOH \cdot H_2O$ (Sigma-Aldrich) were mixed with 60 ml of DI water. The 80 ml of mixture was transferred to an autoclave and subsequently heated at 160°C for 12 hours. After hydrothermal treatment, the resulting precipitates were filtered and washed with distilled water. After the autoclave was cooled to room temperature, the product was dried in an oven at 60°C for 12 hours. Last, the product was heated in a furnace at 200°C for 3 hours under an air atmosphere.

The PI/CNT anode materials were synthesized and modified using a previously reported protocol (*42*). In addition, 1,4,5,8-naphthalenetetracarboxylic dianhydride (2.3 mmol) and CNT (0.50 g) were mixed with 4-chlorophenol (40 g) at 55°C under stirring until completely mixed. Ethylenediamine (0.15 ml) was added to the mixture, followed by heating and refluxing at 200°C for 6 hours. The mixture was cooled to room temperature, and the solid product was rinsed with ethanol, followed by vacuum filtration. The product obtained was dried at 300°C under a N_2 atmosphere for 8 hours to remove any residual solvent.

Electrochemical measurements

The electrode was fabricated by spray coating of mixture onto a hot plate at 60°C consisting of active materials (LMO/CNT or PI/CNT), conductive material (super P), and binder (Nafion) in a weight ratio of 8:1:1. The electrodes were cut into rectangular shapes (30 mm by 10 mm). The electrochemical properties of half and full cells were measured using a VSP (Bio-Logic Science Instruments, France) with a 1 M Li_2SO_4 aqueous electrolyte. The Pt electrode and Ag/AgCl electrode were used as the counter and reference electrodes, respectively. The loading density of the active materials was 0.5 mg cm^{-2}. The full cell was performed between 0.0 and 2.2 V at room temperature and measured using a two-electrode system. In addition, the full cell was tested in a beaker cell containing 1 M Li_2SO_4 with continuous bubbling nitrogen to remove any oxygen.

Packaging material (35 mm by 40 mm by 1 mm) and a spacer of stretchable full batteries were used for the PDMS. The thin spacer (500 μm) accommodated sufficient space to fill the aqueous electrolyte. The stretchable cathode and anode were attached parallel to the bottom layer using an uncured PDMS solution. Then, the top layer, the spacer, and the bottom layer were assembled using O_2 plasma (CUTE, Femto Science, Korea) treatment. Last, the prepared aqueous electrolyte was carefully injected using a syringe.

Characterization

The mechanical properties of the prepared electrode were measured using a tensile strength tester (DA-01, Petrol LAB, Korea). The specimen was cut into a dog-bone shape, and a tensile strength measurement rate of 10 mm min^{-1} was used. The electrical conductivity was analyzed using a four-point probe machine (FPP-RS8, Dasol Eng., Korea). To reduce the contact resistance, a liquid metal (EGaIn) was thinly applied to the AuPU nanocomposite films. The change in resistance during the strain and release was measured using a multimeter. The crystal structure of the LMO/CNT was characterized by an x-ray diffractometer on a Rigaku D/MAX at 2500 V. The morphology of the electrode and active materials was measured by field-emission SEM (Hitachi S-4800). Transmission electron microscopy (TEM) images were taken in bright-field mode using a JEM-2100 (JEOL, Japan). Fourier transform infrared (FT-IR) spectra of PI/CNT were measured using a Varian 670-IR spectrometer. TGA (Q50, TA Instruments, USA) was used to calculate the mass content of the LMO and PI. In situ SAXS measurements were conducted at the 6D UNIST-PAL (Ulsan National Institute of Science and Technology–Pohang Accelerator Laboratory) beamline of the Pohang Accelerator Laboratory in South Korea. The energy of the x-ray was 11.6 keV (wavelength, λ = 1.0668 Å).

SUPPLEMENTARY MATERIALS

Supplementary material for this article is available at http://advances.sciencemag.org/cgi/content/full/5/7/eaaw1879/DC1

Fig. S1. Schematic illustration and TEM image with a corresponding size distribution histogram of citrate-stabilized Au NPs.
Fig. S2. Characterization of the single layer.
Fig. S3. Resistance and conductivity.
Fig. S4. The specific contents of the Au NPs in the high- and low-gradient multilayer conductors.
Fig. S5. SEM of the 9 L high GAP conductor under strain.
Fig. S6. Cross-sectional SEM of the 9 L high GAP conductor under a strain of 100%.
Fig. S7. High-resolution SEM.
Fig. S8. Finite element analysis of (directional) stress distribution.
Fig. S9. Change of resistance on the top surface of 9 L high GAP multilayer conductors under dynamic stretching between 0% strain (orange region) and different uniaxial strains (green region) during 1000 cycles.
Fig. S10. In situ SAXS analysis.
Fig. S11. Characterization of anode materials.
Fig. S12. Characterization of cathode materials.
Fig. S13. Top-view SEM images of active materials.
Fig. S14. Top-view SEM of active materials on a 9 L high GAP conductor under strain.
Fig. S15. Half-cell test of the cathode and anode.
Fig. S16. Top-view SEM images.
Fig. S17. Galvanostatic charge-discharge curves of the full cell at various current densities.
Fig. S18. Voltage curves of the stretchable full cell as a function of time at various current densities.
Fig. S19. Fatigue test of the stretchable battery under 50% strain over 100 cycles.
Fig. S20. Voltage curves of series stretchable full battery in the voltage range from 0 to 4.0 V as a function of time.
Movie S1. LED bulb operated using a stretchable aqueous lithium-ion battery.

REFERENCES AND NOTES

1. J. A. Rogers, T. Someya, Y. Huang, Materials and mechanics for stretchable electronics. *Science* **327**, 1603–1607 (2010).
2. N. Matsuhisa, M. Kaltenbrunner, T. Yokota, H. Jinno, K. Kuribara, T. Sekitani, T. Someya, Printable elastic conductors with a high conductivity for electronic textile applications. *Nat. Commun.* **6**, 7461 (2015).
3. T. Lee, W. Lee, S.-W. Kim, J. J. Kim, B.-S. Kim, Flexible textile strain wireless sensor functionalized with hybrid carbon nanomaterials supported ZnO nanowires with controlled aspect ratio. *Adv. Funct. Mater.* **26**, 6206–6214 (2016).
4. S. Stauss, I. Honma, Biocompatible batteries—Materials and chemistry, fabrication, applications, and future prospects. *Bull. Chem. Soc. Jpn.* **91**, 492–505 (2018).
5. M. Nishizawa, Soft, wet and ionic microelectrode systems. *Bull. Chem. Soc. Jpn.* **91**, 1141–1149 (2018).
6. W. Liu, M.-S. Song, B. Kong, Y. Cui, Flexible and stretchable energy storage: Recent advances and future perspectives. *Adv. Mater.* **29**, 1603436 (2017).
7. W.-J. Song, J. Park, D. H. Kim, S. Bae, M.-J. Kwak, M. Shin, S. Kim, S. Choi, J.-H. Jang, T. J. Shin, S. Y. Kim, K. Seo, S. Park, Jabuticaba-inspired hybrid carbon filler/polymer electrode for use in highly stretchable aqueous Li-ion batteries. *Adv. Energy Mater.* **8**, 1702478 (2018).
8. N. Liu, A. Chortos, T. Lei, L. Jin, T. R. Kim, W.-G. Bae, C. Zhu, S. Wang, R. Pfattner, X. Chen, R. Sinclair, Z. Bao, Ultratransparent and stretchable graphene electrodes. *Sci. Adv.* **3**, e1700159 (2017).
9. K. Kim, J. Kim, B. G. Hyun, S. Ji, S.-Y. Kim, S. Kim, B. W. An, J.-U. Park, Stretchable and transparent electrodes based on in-plane structures. *Nanoscale* **7**, 14577–14594 (2015).
10. L. Hu, M. Pasta, F. La Mantia, L. Cui, S. Jeong, H. D. Deshazer, J. W. Choi, S. M. Han, Y. Cui, Stretchable, porous, and conductive energy textiles. *Nano Lett.* **10**, 708–714 (2010).
11. K.-Y. Chun, Y. Oh, J. Rho, J.-H. Ahn, Y.-J. Kim, H. R. Choi, S. Baik, Highly conductive, printable and stretchable composite films of carbon nanotubes and silver. *Nat. Nanotechnol.* **5**, 853–857 (2010).
12. N. Matsuhisa, D. Inoue, P. Zalar, H. Jin, Y. Matsuba, A. Itoh, T. Yokota, D. Hashizume, T. Someya, Printable elastic conductors by in situ formation of silver nanoparticles from silver flakes. *Nat. Mater.* **16**, 834–840 (2017).
13. M. J. Catenacci, C. Reyes, M. A. Cruz, B. J. Wiley, Stretchable conductive composites from Cu-Ag nanowire felt. *ACS Nano* **12**, 3689–3698 (2018).
14. Y. Kim, J. Zhu, B. Yeom, M. Di Prima, X. Su, J.-G. Kim, S. J. Yoo, C. Uher, N. A. Kotov, Stretchable nanoparticle conductors with self-organized conductive pathways. *Nature* **500**, 59–63 (2013).
15. L. Lopez, Y. Kim, L. Jierry, J. Hemmerle, F. Boulmedais, P. Schaaf, S. Pronkin, N. A. Kotov, Electrochemistry on stretchable nanocomposite electrodes: Dependence on strain. *ACS Nano* **12**, 9223–9232 (2018).
16. K. D. Harris, A. L. Elias, H.-J. Chung, Flexible electronics under strain: A review of mechanical characterization and durability enhancement strategies. *J. Mater. Sci.* **51**, 2771–2805 (2016).
17. C. J. Yu, C. Masarapu, J. P. Rong, B. Q. Wei, H. Q. Jiang, Stretchable supercapacitors based on buckled single-walled carbon nanotube macrofilms. *Adv. Mater.* **21**, 4793–4797 (2009).
18. D.-H. Kim, J. Song, W. M. Choi, H.-S. Kim, R.-H. Kim, Z. Liu, Y. Y. Huang, K.-C. Hwang, Y.-w. Zhang, J. A. Rogers, Materials and noncoplanar mesh designs for integrated circuits with linear elastic responses to extreme mechanical deformations. *Proc. Natl. Acad. Sci. U.S.A.* **105**, 18675–18680 (2008).
19. J. Mu, C. Hou, G. Wang, X. Wang, Q. Zhang, Y. Li, H. Wang, M. Zhu, An elastic transparent conductor based on hierarchically wrinkled reduced graphene oxide for artificial muscles and sensors. *Adv. Mater.* **28**, 9491–9497 (2016).
20. F. Xu, X. Wang, Y. Zhu, Y. Zhu, Wavy ribbons of carbon nanotubes for stretchable conductors. *Adv. Funct. Mater.* **22**, 1279–1283 (2012).
21. J. Zang, C. Cao, Y. Feng, J. Liu, X. Zhao, Stretchable and high-performance supercapacitors with crumpled graphene papers. *Sci. Rep.* **4**, 6492 (2014).
22. S. Xu, Y. Zhang, J. Cho, J. Lee, X. Huang, L. Jia, J. A. Fan, Y. Su, J. Su, H. Zhang, H. Cheng, B. Lu, C. Yu, C. Chuang, T.-i. Kim, T. Song, K. Shigeta, S. Kang, C. Dagdeviren, I. Petrov, P. V. Braun, Y. Huang, U. Paik, J. A. Rogers, Stretchable batteries with self-similar serpentine interconnects and integrated wireless recharging systems. *Nat. Commun.* **4**, 1543 (2013).
23. Y. Arafat, I. Dutta, R. Panat, Super-stretchable metallic interconnects on polymer with a linear strain of up to 100%. *Appl. Phys. Lett.* **107**, 081906 (2015).
24. C. Pan, K. Kumar, J. Li, E. J. Markvicka, P. R. Herman, C. Majidi, Visually imperceptible liquid-metal circuits for transparent, stretchable electronics with direct laser writing. *Adv. Mater.* **30**, 1706937 (2018).
25. R. Libanori, R. M. Erb, A. Reiser, H. Le Ferrand, M. J. Süess, R. Spolenak, A. R. Studart, Stretchable heterogeneous composites with extreme mechanical gradients. *Nat. Commun.* **3**, 1265 (2012).
26. J. Lyu, M. D. Hammig, L. Liu, L. Xu, H. Chi, C. Uher, T. Li, N. A. Kotov, Stretchable conductors by kirigami patterning of aramid-silver nanocomposites with zero conductance gradient. *Appl. Phys. Lett.* **111**, 161901 (2017).

27. G. Decher, Fuzzy nanoassemblies: Toward layered polymeric multicomposites. *Science* **277**, 1232–1237 (1997).
28. J. J. Richardson, M. Björnmalm, F. Caruso, Technology-driven layer-by-layer assembly of nanofilms. *Science* **348**, aaa2491 (2015).
29. T. Lee, S. H. Min, M. Gu, Y. K. Jung, W. Lee, J. U. Lee, D. G. Seong, B.-S. Kim, Layer-by-layer assembly for graphene-based multilayer nanocomposites: Synthesis and applications. *Chem. Mater.* **27**, 3785–3796 (2015).
30. M. Gu, B.-S. Kim, Unraveling the importance of controlled architecture in bimetallic multilayer electrode toward efficient electrocatalyst. *Nano Energy* **30**, 658–666 (2016).
31. G. Rydzek, Q. Ji, M. Li, P. Schaaf, J. P. Hill, F. Boulmedais, K. Ariga, Electrochemical nanoarchitectonics and layer-by-layer assembly: From basics to future. *Nano Today* **10**, 138–167 (2015).
32. J. Zhu, H. Zhang, N. A. Kotov, Thermodynamic and structural insights into nanocomposites engineering by comparing two materials assembly techniques for graphene. *ACS Nano* **7**, 4818–4829 (2013).
33. P. Podsiadlo, M. Qin, M. Cuddihy, J. Zhu, K. Critchley, E. Kheng, A. K. Kaushik, Y. Qi, H.-S. Kim, S.-T. Noh, E. M. Arruda, A. M. Waas, N. A. Kotov, Highly ductile multilayered films by layer-by-layer assembly of oppositely charged polyurethanes for biomedical applications. *Langmuir* **25**, 14093–14099 (2009).
34. N. A. Kotov, I. Dékány, J. H. Fendler, Ultrathin graphite oxide-polyelectrolyte composites prepared by self-assembly: Transition between conductive and non-conductive states. *Adv. Mater.* **8**, 637–641 (1996).
35. S. Stankovich, D. A. Dikin, G. H. B. Dommett, K. M. Kohlhaas, E. J. Zimney, E. A. Stach, R. D. Piner, S. T. Nguyen, R. S. Ruoff, Graphene-based composite materials. *Nature* **442**, 282–286 (2006).
36. B. Liu, L. Huang, L. Geng, F. Yin, [Multiscale Hierarchical Structure and Laminated Strengthening and Toughening Mechanisms], in *Lamination: Theory and Application*, C. Osheku, Ed. (IntechOpen, 2018), chap. 2, pp. 19–49.
37. K. Kojio, K. Matsuo, S. Motokucho, K. Yoshinaga, Y. Shimodaira, K. Kimura, Simultaneous small-angle X-ray scattering/wide-angle X-ray diffraction study of the microdomain structure of polyurethane elastomers during mechanical deformation. *Polymer J.* **43**, 692–699 (2011).
38. H. Zhang, A. K. Scholz, J. de Crevoisier, F. Vion-Loisel, G. Besnard, A. Hexemer, H. R. Brown, E. J. Kramer, C. Creton, Nanocavitation in carbon black filled styrene-butadiene rubber under tension detected by real time small angle X-ray scattering. *Macromolecules* **45**, 1529–1543 (2012).
39. K. Yamaguchi, J. J. C. Busfield, A. G. Thomas, Electrical and mechanical behavior of filled elastomers. I. The effect of strain. *J. Polym. Sci. B* **41**, 2079–2089 (2003).
40. N. Alias, A. A. Mohamad, Advances of aqueous rechargeable lithium-ion battery: A review. *J. Power Sources* **274**, 237–251 (2015).
41. Y. Zhao, Y. Ding, Y. Li, L. Peng, H. R. Byon, J. B. Goodenough, G. Yu, A chemistry and material perspective on lithium redox flow batteries towards high-density electrical energy storage. *Chem. Soc. Rev.* **44**, 7968–7996 (2015).
42. Y. Zhang, Y. Wang, L. Wang, C.-M. Lo, Y. Zhao, Y. Jiao, G. Zheng, H. Peng, A fiber-shaped aqueous lithium ion battery with high power density. *J. Mater. Chem. A* **4**, 9002–9008 (2016).
43. Z. Guo, L. Chen, Y. Wang, C. Wang, Y. Xia, Aqueous lithium-ion batteries using polyimide-activated carbon composites anode and spinel $LiMn_2O_4$ cathode. *ACS Sustain. Chem. Eng.* **5**, 1503–1508 (2017).

Acknowledgments: We thank P. Joo and Y. Kim for extensive help and comments on the project. **Funding:** This work was supported by the Center for Advanced Soft Electronics funded by the Ministry of Science, ICT and Future Planning as Global Frontier Project (CASE 2015M3A6A5072945), and the National Research Foundation of Korea (NRF) (NRF-2017R1A2B3012148, NRF-2017M3A7B4052802, NRF-2018R1A5A1025208, and NRF-2018R1A5A1025224). Partial support of this study was also provided by NSF 1463474, NSF 1538180, and AFOSR FA9550-16-1-0265 projects. **Author contributions:** M.G., W.-J.S., S.P., and B.-S.K. participated in conceiving and designing the project. M.G. and W.-J.S. contributed to experimental work and conducted data analysis. J.H. and S.Y.K. designed and conducted computational calculation and simulation. T.J.S. assisted in the SAXS analysis. N.A.K. assisted in the acquisition of PU with critical comments on the project. M.G., W.-J.S., S.P., B.-S.K., and N.A.K. co-wrote the manuscript. **Competing interests:** The authors declare that they have no competing interests. **Data and materials availability:** All data needed to evaluate the conclusions in the paper are present in the paper and/or the Supplementary Materials. Additional data related to this paper may be requested from the authors.

Submitted 27 November 2018
Accepted 20 June 2019
Published 26 July 2019
10.1126/sciadv.aaw1879

Citation: M. Gu, W.-J. Song, J. Hong, S. Y. Kim, T. J. Shin, N. A. Kotov, S. Park, B.-S. Kim, Stretchable batteries with gradient multilayer conductors. *Sci. Adv.* **5**, eaaw1879 (2019).

Science Advances

Stretchable batteries with gradient multilayer conductors

Minsu Gu, Woo-Jin Song, Jaehyung Hong, Sung Youb Kim, Tae Joo Shin, Nicholas A. Kotov, Soojin Park and Byeong-Su Kim

Sci Adv **5** (7), eaaw1879.
DOI: 10.1126/sciadv.aaw1879